Physics in Medicine & Biology

IPEM
Institute of Physics and Engineering in Medicine

PAPER

Experimental evaluation of convolutional neural network-based inter-crystal scattering recovery for high-resolution PET detectors

To cite this article: Seungeun Lee and Jae Sung Lee 2023 *Phys. Med. Biol.* **68** 095017

IOP Publishing Phys. Med. Biol. 68 (2023) 095017 https://doi.org/10.1088/1361-6560/accacb

Physics in Medicine & Biology

IPEM Institute of Physics and Engineering in Medicine

CrossMark

RECEIVED
22 October 2022

REVISED
31 March 2023

ACCEPTED FOR PUBLICATION
5 April 2023

PUBLISHED
26 April 2023

PAPER

Experimental evaluation of convolutional neural network-based inter-crystal scattering recovery for high-resolution PET detectors

Seungeun Lee[1,2] and Jae Sung Lee[1,3]

[1] Department of Nuclear Medicine, Seoul National University, Seoul, 03080, Republic of Korea
[2] Department of Biomedical Sciences, Seoul National University, Seoul, 03080, Republic of Korea
[3] Brightonix Imaging Inc., Seoul, 04782, Republic of Korea

E-mail: jaes@snu.ac.kr

Keywords: inter-crystal scattering, machine learning, convolutional neural network, high-resolution PET, PET detectors

Supplementary material for this article is available online

Abstract

Objective. One major limiting factor for achieving high resolution of positron emission tomography (PET) is a Compton scattering of the photon within the crystal, also known as inter-crystal scattering (ICS). We proposed and evaluated a convolutional neural network (CNN) named ICS-Net to recover ICS in light-sharing detectors for real implementations preceded by simulations. ICS-Net was designed to estimate the first-interacted row or column individually from the 8×8 photosensor amplitudes. *Approach.* We tested 8×8, 12×12, and 21×21 Lu_2SiO_5 arrays with pitches of 3.2, 2.1, and 1.2 mm, respectively. We first performed simulations to measure the accuracies and error distances, comparing the results to previously studied pencil-beam-based CNN to investigate the rationality of implementing fan-beam-based ICS-Net. For experimental implementation, the training dataset was prepared by obtaining coincidences between the targeted row or column of the detector and a slab crystal on a reference detector. ICS-Net was applied to the detector pair measurements with moving a point source from the edge to center using automated stage to evaluate their intrinsic resolutions. We finally assessed the spatial resolution of the PET ring. *Main results.* The simulation results showed that ICS-Net improved the accuracy compared with the case without recovery, reducing the error distance. ICS-Net outperformed a pencil-beam CNN, which provided a rationale to implement a simplified fan-beam irradiation. With the experimentally trained ICS-Net, the degree of improvements in intrinsic resolutions were 20%, 31%, and 62% for the 8×8, 12×12, and 21×21 arrays, respectively. The impact was also shown in the ring acquisitions, achieving improvements of 11%–46%, 33%–50%, and 47%–64% (values differed from the radial offset) in volume resolutions of 8×8, 12×12, and 21×21 arrays, respectively. *Significance.* The experimental results demonstrate that ICS-Net can effectively improve the image quality of high-resolution PET using a small crystal pitch, requiring a simplified setup for training dataset acquisition.

1. Introduction

The imaging performance of positron emission tomography (PET) relies on the capability of the detector to measure the time, energy, and position of the interaction of a 511 keV photon originating from the positron emitter. Precise measurement of the time-of-flight (TOF) enables localization of the source position within the field of view (FOV), dramatically enhancing the signal-to-noise ratio of the images with TOF reconstruction (Conti 2011, Surti and Karp 2016). Good energy resolution enables the effective extraction of 511 keV events and quantitative corrections that utilize energy information (Koral *et al* 1990, Shao *et al* 1994). Accurate event positioning is essential for achieving superior spatial resolution (Surti and Karp 2018). The complicated relationships between time, energy, and position measurements are optimized with the detector design and material selection depending on the imaging target of the PET scanner.

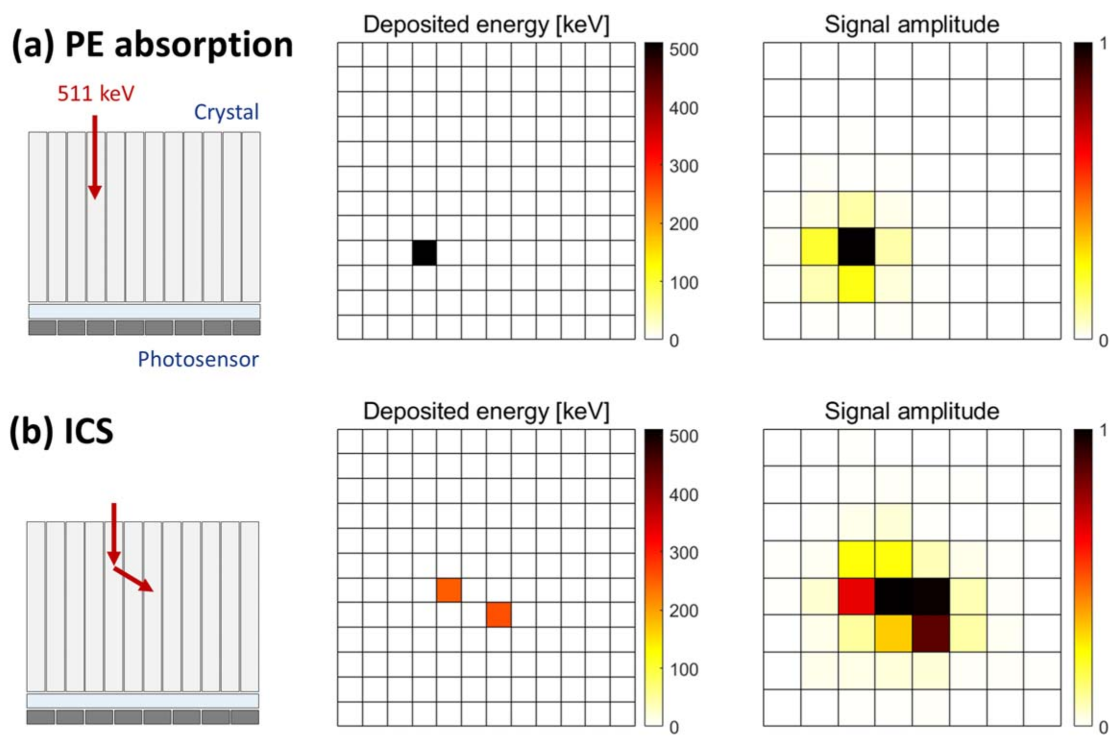

Figure 1. Schematics of (a) PE absorption and (b) ICS event in a 12 × 12 crystal array coupled to an 8 × 8 photosensor array occurred by a perpendicularly irradiated single 511 keV photon. The true deposited energy in the pixelated crystal array and the corresponding signal amplitude from the photosensor are shown in order. ICS is an event in which a 511 keV photon deposits its energy in multiple crystals due to Compton scattering. PE: photoelectric, ICS: inter-crystal scattering.

Although significant efforts have been made to develop high-end detector hardware in recent decades, machine learning (ML) has recently been highlighted as a promising approach (Gong *et al* 2020, Arabi *et al* 2021, Ullah and Levin 2022). ML has been established as a major technique in nuclear medicine imaging to overcome high noise and enhance the quantification performance (Kim *et al* 2019, Lee *et al* 2019, Yie *et al* 2020, Hwang *et al* 2021, Kang *et al* 2021). At the detector level, the general role of ML is to extract valuable representations from minimal sampling capabilities. The timing uncertainty is effectively reduced by estimating the photon arrival time with ML using the scintillation signals sampled by oscilloscopes or digitizers (Berg and Cherry 2018, Kwon *et al* 2021, Onishi *et al* 2022). Neural networks are popular techniques for 3D positioning of photon interactions within monolithic crystals; these networks utilize the distributions of light detected by sparsely aligned photosensors (Muller *et al* 2019, Peng *et al* 2019, Sanaat and Zaidi 2020, Gonzalez-Montoro *et al* 2021).

Inter-crystal scattering (ICS) is one of the major factors limiting the positioning accuracy of detectors of which the effect also can be mitigated by using ML. Unlike photoelectric (PE) interactions, an ICS event involves two or more energy depositions via Compton scattering within the scintillator block, resulting in incorrect positioning of the first interaction (Shao *et al* 1996, Miyaoka and Lewellen 2000, Gu *et al* 2010, Ritzer *et al* 2017, Hsu *et al* 2019, Teimoorisichani and Goertzen 2019, Zhang *et al* 2019, Kang *et al* 2021) (figure 1). ICS is unavoidable because of the substantial cross-sections of the crystal materials for Compton scattering of 511 keV photons, which highlights the importance of ICS recovery. Here, the term 'ICS recovery' indicates recovering the sequence of the photon interactions in an ICS event to find the first interaction. The methodologies to recover ICS have been proposed by a number of groups (Abbaszadeh *et al* 2018, Yang *et al* 2018, Ritzer *et al* 2020) including ML (Wu *et al* 2020, Nasiri and Abbaszadeh 2021). Some studies experimentally showed the impact of ML approach on ICS in real detectors. One good example is support vector machine which showed good classification ability of the photon interaction types based on the light distributions to reject the ICS events (Yoshida *et al* 2007). However, rejecting a significant amount of events would lead to a loss in signal-to-noise of the system. Another group implemented a pre-trained network on a field-programmable gate array to recover multiple coincidences caused by Compton scatterings (Michaud *et al* 2015). Both aforementioned studies utilized Monte Carlo data for training and then applied the trained model to real detectors or systems, showing improvements in image quality. However, the appropriateness of preparing supervising data with simulation is questionable because the performance of ML is expected to be dependent on how effectively the simulations reflected the reality. The experimental implementation of ML for ICS recovery of light-sharing detectors needs to be further studied.

A concept of employing the convolutional neural network (CNN) for recovering ICS events in various pixelated crystal arrays was proposed in our previous study (Lee and Lee 2021). With extensive simulations, the impacts of CNN on recovery accuracy and spatial resolution were evaluated. We focused on light-sharing detectors because ICS accounts for a high portion of the events in these detectors, while identifying the interactions is challenging compared to 1-to-1 coupled detectors due to the multiplexed signals from the interacting crystals. The proposed method features event-by-event processing at the detector level and utilizes the entire ICS events to maintain sensitivity, rather than rejecting them. When fed with a photosensor signal array, the CNN so-called ICS-cNet estimated the first-interacted crystal, resulting in an improvement in the spatial resolution of PET comprising highly pixelated detectors. Still, the absence of experimental data remained a limitation.

Building on prior research, this study extends to demonstrate the performance enhancement of real detectors with CNN. We trained the network with experimental data to account for the detector characteristics which substantially differed from the ideal conditions of the Monte Carlo simulations. The original ICS-cNet required the labeling of every crystal using pencil-beam irradiation to identify the first interaction, which would be burdensome in reality. Therefore, we modified the network to select the first-interacted row or column of the crystal array, reducing the number of data acquisitions from N^2 to 2 N for the $N \times N$ crystal array. Prior to experiments, we conducted simulations to validate the rationale of using this modified network, named ICS-Net, by comparing its performance with that of previous ICS-cNet. By combining the simulation results and the findings in the previous study that shows spatial resolution improvements, replacing ICS-cNet with ICS-Net for the experiments was justified. For the experimental setup, we assembled the detector arrays and acquired training datasets using a slab crystal to function as a fan beam, irradiating a specific row or column. We then evaluated the ICS-Net by measuring the intrinsic resolution of the detector pair and the spatial resolution of the pseudo-PET ring constructed with a detector pair.

2. Materials and methods

2.1. Crystal arrays

We tested three different polished Lu_2SiO_5 (LSO) crystal arrays which differed in pitch and width of the crystal elements with 20 mm crystal length. The 8×8, 12×12, and 21×21 arrays consisted of crystal elements with widths of 3.0, 2.0, and 1.08 mm and pitches of 3.2, 2.1, and 1.2 mm, respectively. The side view of a 12×12 array is depicted in figure 3 for example. Diffusive reflectors were placed between the crystal elements and the outer crystal block. The total crystal block size, including the crystals and reflectors, was 25.8 mm $\times$ 25.8 mm $\times$ 20 mm for all the crystal arrays. The occurrence rates of ICS are 34%, 39%, and 44% for 8×8, 12×12, and 21×21 arrays, respectively (Lee and Lee 2021).

2.2. ICS-Net

2.2.1. Input and structure

The proposed ICS-Net uses an 8×8 array of signal amplitudes measured by the photosensor as input to predict the row or column index of the first-interacted crystal (figure 2(a)). Here, the input is the number of optical photons detected by 8×8 photosensitive areas normalized with the maximum amplitude. The selected 511 keV photopeak events contain both PE and ICS, undistinguished. The network consists of two convolutional layers and a fully-connected layer at the end to choose one of the N rows or columns.

2.2.2. Network training

ICS-Net-R (row) and ICS-Net-C (column) were individually trained with the same hyperparameters. Adam optimizer and cross-entropy loss were used for the network training. The learning rate was initially set as 0.001 and it was dropped by a factor of 0.1 every epoch. The number of channels for two layers (C_1, C_2) was optimized as (60, 180), (60, 240), and (70, 350) for the 8×8, 12×12, and 21×21 arrays, respectively, while the number of epochs was 20 for all arrays. In an ideal symmetric case (e.g. simulation), ICS-Net-R (row) and ICS-Net-C (column) can share one network, whereas experimental studies require individual training of ICS-Net-R and ICS-Net-C for several factors. As shown in figure 2(b), both loss function and accuracy converged well, which implies that the network shows good stability.

ICS-Net is a modified version of ICS-cNet designed and tested in a previous study (Lee and Lee 2021). ICS-cNet directly selects the first interaction among the N^2 crystals. Therefore, the output vector size was $N^2 \times 1$, and the overall structure was identical to that of the ICS-Net.

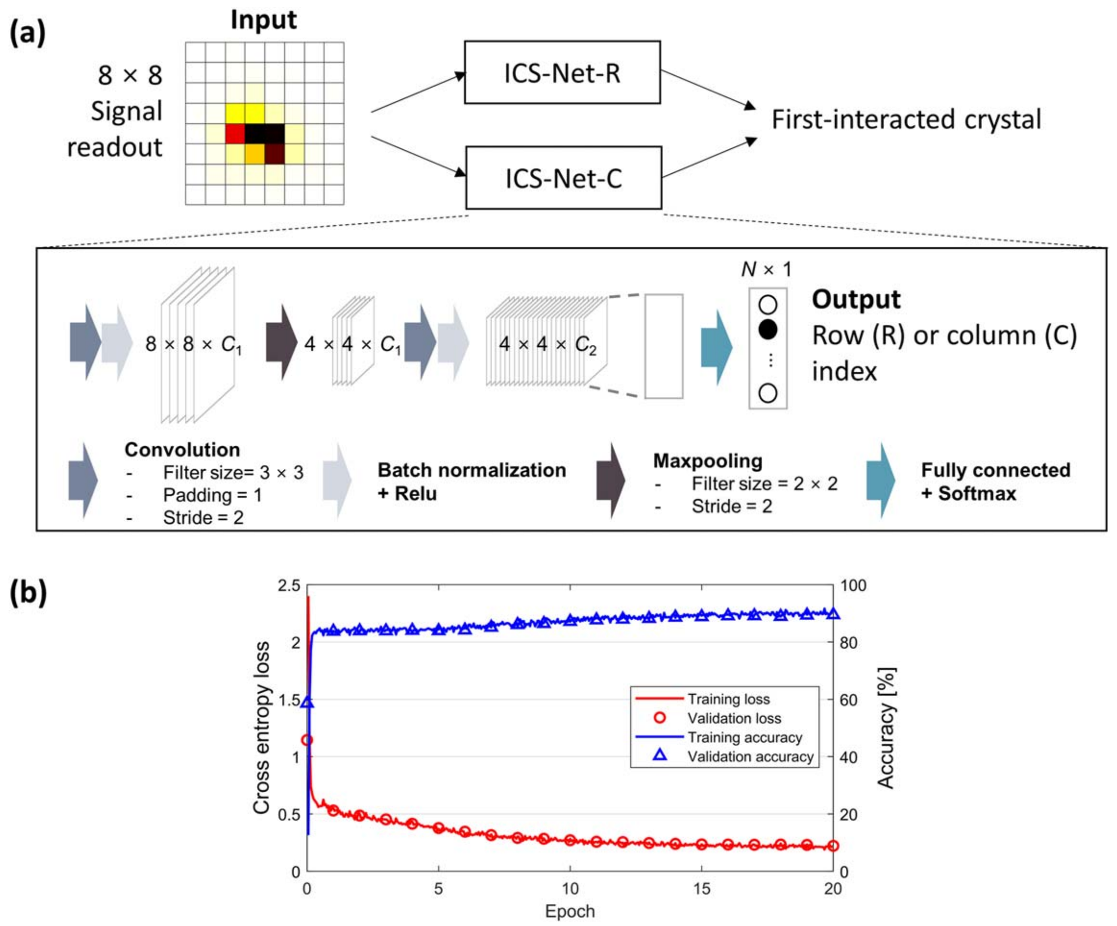

Figure 2. Structure and training of ICS-Net. (a) Schematic of applying ICS-Net for ICS recovery using the 8×8 signal array. The first-interacted row and column were individually determined with the respective network. The structure of the ICS-Net-R (row) or ICS-Net-C (column) is shown below. C_1 and C_2 denote the optimized number of channels. (b) Loss and accuracy as function of epochs during the training (example of ICS-Net-R for 8×8 array simulation).

2.3. Simulation

2.3.1. GATE setup

We first investigated the feasibility of ICS-Net using GATE v8.2 Monte Carlo and UNIFIED optical simulation (Levin and Moisan 1996, Jan *et al* 2004). The density, refractive index, and light yield of the LSO were 7.4 g cm^{-3}, 1.82, and 26 000 MeV^{-1} respectively. The photosensor consisted of an 8×8 array of 3 mm × 3 mm photosensitive areas in a 3.2 mm pitch. A 25.8 mm × 25.8 mm × 1.5 mm epoxy light guide was placed to diffuse the scintillation photons from the crystal elements to the photosensor. The intrinsic uncertainty of optical photon emission of LSO material was 9% in FWHM at 511 keV. The surfaces of the crystals and light guide were polished ($\sigma_\alpha = 0.1°$), 5 sides wrapped by a diffusive reflector with 98% reflectivity. We used *Hits* output of GATE to analyze every photon interaction and manually applied an energy threshold of 400 keV. To generate training and test datasets, the entire array was uniformly and perpendicularly irradiated by 511 keV photons from the top side. The number of events per row or column was about 20 000 × N in total for the $N \times N$ array. 75%, 10%, and 15% of the datasets were used for training, validation, and testing, respectively. *Photoelectric* and *Compton* processes were enabled for 511 keV photon interaction using the standard model, while *Scintillation*, *OpticalAbsorption*, and *OpticalBoundary* were enabled for optical photon generation and tracking.

2.3.2. Evaluation of simulated data

By applying the trained ICS-Net to the test dataset as described in section 2.2, we measured the accuracies for selecting the first-interacted crystals for each ICS, PE, and total (ICS + PE) event. We also measured the error distance between the centers of the true first-interacted crystal and the network output and calculated the 2D root mean square error distance (RMSED) for the total events as follows:

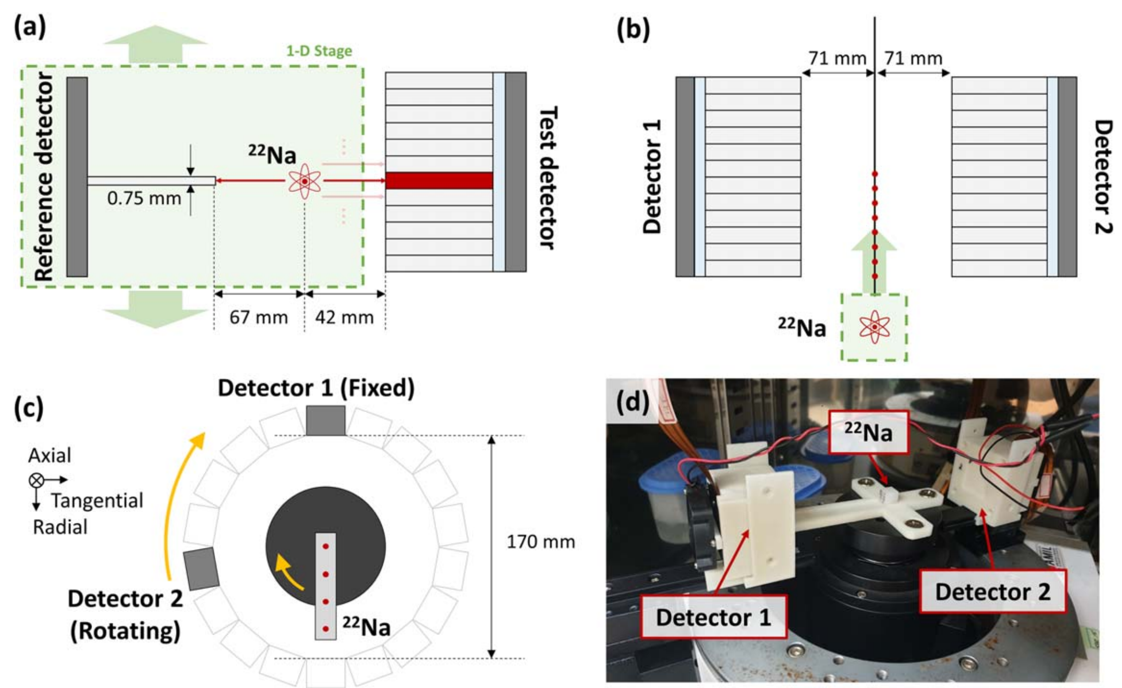

Figure 3. Experimental setup for evaluation of ICS-Net. (a) Training dataset acquisition, (b) intrinsic resolution measurement, and (c) spatial resolution measurement (also shown with the photograph (d)).

$$\mathrm{RMSED} = \sqrt{\frac{1}{N}\sum_{n=1}^{N}((x_{\mathrm{pred},n} - x_{\mathrm{true},n})^2 + (y_{\mathrm{pred},n} - y_{\mathrm{true},n})^2)}, \tag{1}$$

where $(x, \ y)$ indicates 2D position of the true or predicted (with or without ICS-Net) crystal for the n th event, and N indicates the total number of the test events.

Another metric, the relative RMSED reduction ($\mathrm{RMSED_{red}}$), was calculated to evaluate the impact of ICS-Net relative to the crystal pitch because the pitch intrinsically determines the spatial resolution (the value with the notation *No recov* is later explained in section 2.5):

$$\mathrm{RMSED_{red}} = \frac{\mathrm{RMSED_{No\ recov}}[\mathrm{mm}] - \mathrm{RMSED_{ICS-Net}}[\mathrm{mm}]}{\mathrm{Crystal\ pitch\ [mm]}}. \tag{2}$$

These measurements were compared with those of ICS-cNet presented in a previous study (Lee and Lee 2021) using the identical datasets.

2.4. Experiment

2.4.1. Training dataset acquisition

The test detectors were assembled using an LSO array (Meishan Boya Advanced Materials, China), a 32 mm × 32 mm × 2 mm acrylic light guide, and a digital photon counter (DPC; DPC-3200–22–44; Philips, USA). A reference detector was also assembled by coupling a 0.75 mm LSO slab crystal to another DPC. The number of scintillation photons detected by the 8 × 8 DPC pixels was individually read out using the Philips Technical Evaluation Kit with a full-tile neighbor logic enabled (Schulze 2013).

The training and test datasets were acquired using electronic collimation, as shown in figure 3(a). To irradiate the known first-interacted single row or column of the test crystal array, we acquired coincidence data between the test and reference detectors with a ^{22}Na point source placed between the target row or column and the slab crystal. The distance from the point source to the test and reference crystals were 42 mm and 67 mm, respectively. The effective beam width entering the top of the test detector was then calculated to be 0.47 mm using the ratio of similitude. The reference detector and point source were mounted on a 1D motorized stage to automatically irradiate each row or column in a step size equal to the crystal pitch. An energy window of 511 keV ± FWHM/2 was applied to the dataset, where FWHM indicates the global energy resolution of the test detector in full-width at half-maximum (19%, 23%, and 31% for 8 × 8, 12 × 12, and 21 × 21, respectively). Approximately 80 000 coincidence events were acquired after energy windowing for every row or column. To enlarge the dataset and prevent overfitting, a 2-fold augmentation for ICS-Net-R was performed by flipping the dataset row-wise and assigning them to the same first-interacted row. The same procedure was repeated for ICS-Net-C.

The acquired events were used to train (80%), validation (10%) and test (10%) ICS-Net-R and ICS-Net-C of each crystal array to counter the asymmetric geometry of the DPC channel areas. The networks were trained and applied individually for each detector to counter the differences in the DPC characteristics such as gain and dark count rate. The entire experiment was conducted in a temperature-controlled box at 10 °C.

2.4.2. Intrinsic resolution measurement

To evaluate the impact of the ICS-Net on the detector level, we measured the intrinsic resolution using the setup shown in figure 3(b). A 1D motorized stage was placed at the middle of the facing detector pair to move a ^{22}Na point source from one edge to the center. The moving step sizes were 0.5, 0.35, and 0.2 mm for 8×8, 12×12, and 21×21 test detectors, respectively. The trained ICS-Net-R and ICS-Net-C models were applied to the acquired events to determine the first-interacted crystals. The FWHMs and full-width at tenth-maxima (FWTMs) of the count profiles acquired by the opposing crystal pairs were measured and averaged for each test detector pair.

The degree of improvement in the intrinsic resolution was compared. The intrinsic resolution (R_{intr}) was modelled as follows:

$$R_{\mathrm{intr}} = \sqrt{R_{\mathrm{det}}^2 + R_{\mathrm{range}}^2 + R_{180\circ}^2 + R_{\mathrm{blur}}^2}\,, \tag{3}$$

where R_{det}, R_{range}, $R_{180\circ}$, and R_{blur} are the resolution determined by crystal pitch, positron range, nonlinearity of annihilation photon emissions, and blurring factors including ICS, crystal misidentification, and crystal penetration (Rahmim *et al* 2013). We expect to reduce R_{blur} by applying ICS-Net in this study. The R_{intr} improvement was calculated as follows:

$$R_{\mathrm{intr}}\,\mathrm{improvement}\ [\%] = \frac{\sqrt{R_{\mathrm{intr,No\ recov}}^2 - R_{\mathrm{intr,ICS-Net}}^2}}{R_{\mathrm{intr,No\ recov}}} \times 100. \tag{4}$$

Because the numerator of the right-hand side is equal to $\sqrt{R_{\mathrm{blur,\ No\ recov}}^2 - R_{\mathrm{blur,ICS-Net}}^2}$, the metric R_{intr} improvement indicates the reduction of ICS blurring relative to the resolution without ICS recovery.

2.4.3. Spatial resolution measurement

A pair of detectors as mounted on a 2-axis rotational stage to construct a virtual PET ring prototype (figures 3(c), (d)). The outer axis rotated one detector whereas the other detector was fixed to imitate the relative placement of the two detectors. The inner axis rotated the imaging target to imitate the relationship between the target and detector pair. Data were acquired for every pair of outer- and inner-axis placements. The virtual ring consisted of 18 transaxial detectors and one axial detector; thus, the crystal face-to-face distance and axial length of the ring were 170 mm and 25.8 mm, respectively.

The spatial resolution of the prototype ring was measured using a 3.9 μCi ^{22}Na point source with a 0.25 mm radius encapsulated in a 10 mm plastic cube. The radial offsets of the point source were 0, 2, 4, and 6 cm. Data were acquired for 3 min for each detector placement pair. Image reconstruction was based on 3D ordered-subset expectation maximization with 1 iteration and 18 subsets. Because the point source size was negligible compared to the image voxel and the attenuation due to the embedding cube was negligible, we did not apply image corrections such as normalization and attenuation corrections for the spatial resolution measurement. Finally, the volumetric resolution ($\mathrm{FWHM}_{\mathrm{vol}}$) and its improvement were calculated as follows:

$$\mathrm{FWHM}_{\mathrm{vol}}[\mathrm{mm}^3] = \mathrm{FWHM}_{\mathrm{rad}}[\mathrm{mm}] \times \mathrm{FWHM}_{\mathrm{tan}}[\mathrm{mm}] \times \mathrm{FWHM}_{\mathrm{axl}}[\mathrm{mm}] \tag{5}$$

$$\mathrm{FWHM}_{\mathrm{vol}}\ \mathrm{improvement}[\%] = \frac{\mathrm{FWHM}_{\mathrm{vol,No\ recovery}} - \mathrm{FWHM}_{\mathrm{vol,ICS-Net}}}{\mathrm{FWHM}_{\mathrm{vol,No\ recovery}}} \times 100\%, \tag{6}$$

where $\mathrm{FWHM}_{\mathrm{rad}}$, $\mathrm{FWHM}_{\mathrm{tan}}$, and $\mathrm{FWHM}_{\mathrm{axl}}$ denote the radial, tangential, and axial resolutions, respectively, in the FWHM.

2.5. Comparison with the case of no recovery applied

Throughout the simulations and experiments, the results of ICS-Net were compared with a practical flood map-based crystal assignment, which corresponded to the case without ICS recovery. For each detector, the 2D flood map was generated by weighting the 8×8 output amplitudes to the respective positions of the photosensor (DPC) pixels, and integrating the events over the entire irradiations in training data acquisition. Examples of the flood maps are presented in figure 4. A Voronoi diagram was drawn based on the crystal peaks on the map, and the segments were indexed sequentially. Most of the PE absorptions were populated on the peak, while ICS appeared between the peaks owing to energy depositions in multiple crystals. Once generated, the flood map was used as a template to assign the crystal index for every upcoming event.

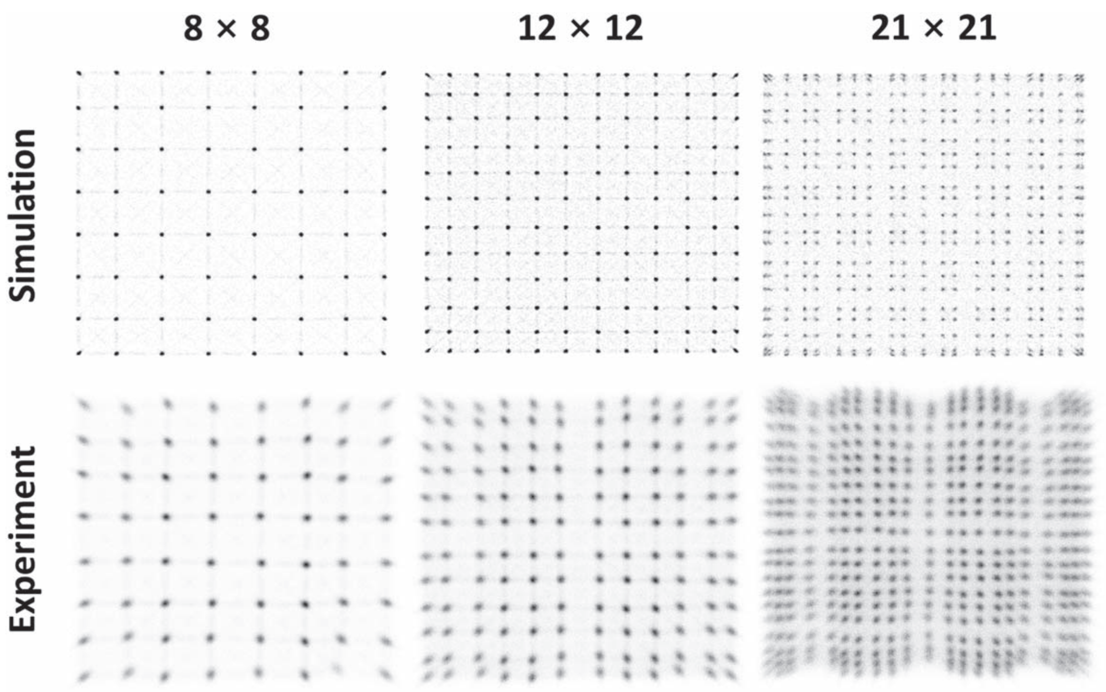

Figure 4. Flood maps of 8 × 8, 12 × 12, and 21 × 21 detectors obtained from simulation (upper) and experiment (lower), which are practically used for event positioning without ICS recovery.

3. Results

3.1. Simulation

3.1.1. Detector-level evaluation

ICS-Net yielded approximately two times higher accuracy in selecting the first-interacted crystals of the ICS events compared to the case of no recovery applied, whereas the crystals of PE events were almost 100% correctly selected for all configurations (figure 5(a)). Concerning the total events, ICS + PE, ICS-Net yielded accuracy increments of 10% for all crystal arrays, whereas ICS accounted for 34%, 39%, and 43% of the total events for the 8 × 8, 12 × 12, and 21 × 21 arrays, respectively (Lee and Lee 2021). The accuracy was relatively low for the highly light-shared array because the photosensor response was insensitive to the difference in the interaction schemes, making it challenging for the network to learn the pattern accurately. The closely located crystals on the simulated flood map of the 21 × 21 array shown in figure 4 support this explanation.

Owing to its high accuracy in finding the first interaction, ICS-Net reduced the RMSED of crystal positioning, implying a reduction in spatial blurring compared with the case without recovery for all arrays (figure 5(b)). A considerable impact of ICS-Net on the small-pitch array can be expected with a high $\mathrm{RMSED}_{\mathrm{red}}$ which was defined in equation (2).

Compared with ICS-cNet from a previous study, ICS-Net exhibited lower accuracy in determining the exact indices of the first-interacted crystals. In contrast, ICS-Net showed smaller RMSED and higher RMSED_{red} than ICS-cNet, indicating better improvements in spatial resolution. In figure 6, the normalized cumulative density functions (CDFs) of the error distance between the true and assigned crystals saturated into 1 more rapidly for ICS-Net than ICS-cNet. The results imply that the crystals were assigned closer to the true first-interacted crystals for false events with ICS-Net despite its small degradation in accuracy (corresponding to the probability at error distance = 0 mm). We assume that individual prediction of rows and columns in ICS-Net served as a double sampling of the signal output, which utilizes twice as much information as ICS-cNet. Additionally, the probability of overfitting is expected to be lowered because ICS-Net can encode first-interacted row (column) output from various first-interacted column (row), consequently requiring fewer output labels than ICS-cNet.

3.2. Experiment

3.2.1. Training dataset acquisition

Figure 7 shows examples of irradiating a single row of test detectors for labeling. For every acquisition, we confirmed the geometrical alignment of the setup by generating a flood map. The bold peaks in the line indicate

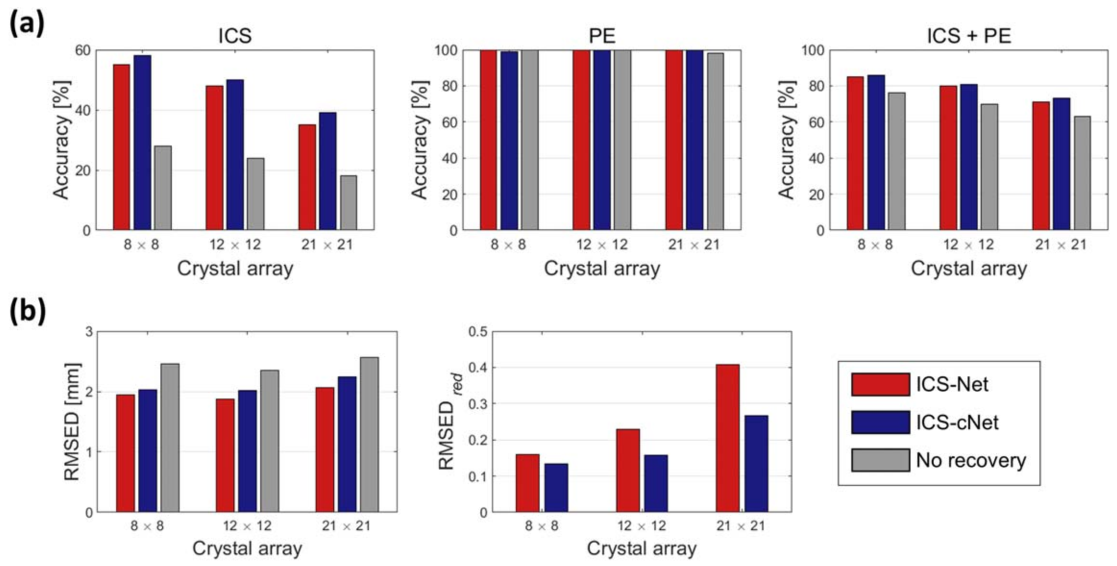

Figure 5. Simulation results of (a) accuracy and (b) RMSED of ICS-Net, ICS-cNet, and no recovery applied.

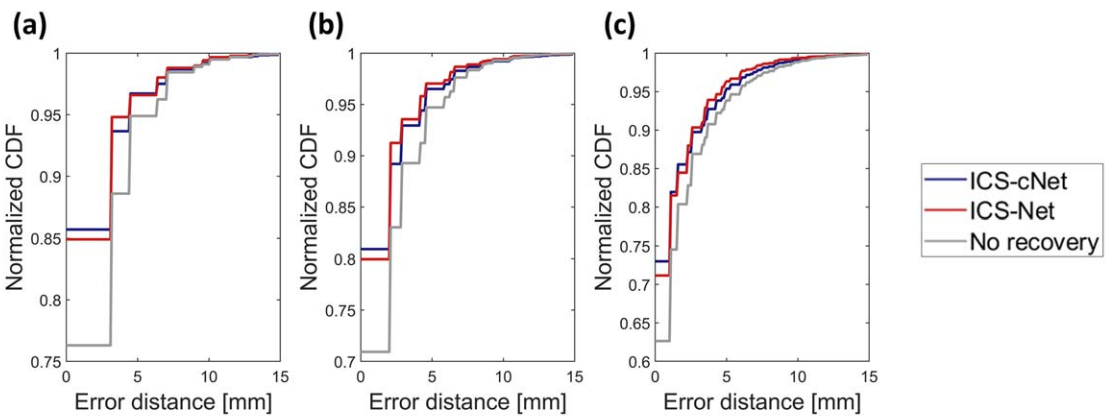

Figure 6. Normalized CDFs of error distance from the true first-interacted crystal by applying ICS-cNet, ICS-Net, and without recovery to (a) 8 × 8, (b) 12 × 12, and (c) 21 × 21 detectors.

the irradiated crystals in the labeled row. The peaks in the adjacent rows also appeared, more significantly for the smaller-pitch array. Wrong irradiation owing to the limitation in the precision of the detector alignment would have contributed to these peaks along with ICS events sharing the energy largely with the adjacent rows.

3.2.2. Intrinsic resolution

ICS-Net exhibited shaper count profiles with higher profile intensities than the case of no recovery (figure 8), indicating the decrease in count leakage into other crystal pairs due to mispositioning. Consequently, reductions in the FWHM and FWTM were observed by applying ICS-Net (table 1). The R_{intr} improvement due to ICS recovery was higher for the smaller-pitch array, which was in good agreement with the findings in the simulation. ICS-Net effectively alleviated ICS blurring for small-pitch arrays, where the ICS accounted for a large proportion of the photon interaction types. In addition, the practical flood map-based assignment for the 21 × 21 array was degraded with poor flood map quality of which the crystals were hardly resolved as shown in figure 4.

3.2.3. Spatial resolution

The reconstructed images and measured FWHM and FWTM values of the ^{22}Na point source acquisitions for various radial offsets are shown in figure 9. A reduction in the tangential blurring was well observed, particularly

Figure 7. Examples of irradiating a single row of the (a) 8 × 8, (b) 12 × 12, and (c) 21 × 21 arrays using a slab crystal for labeling the first-interacted row.

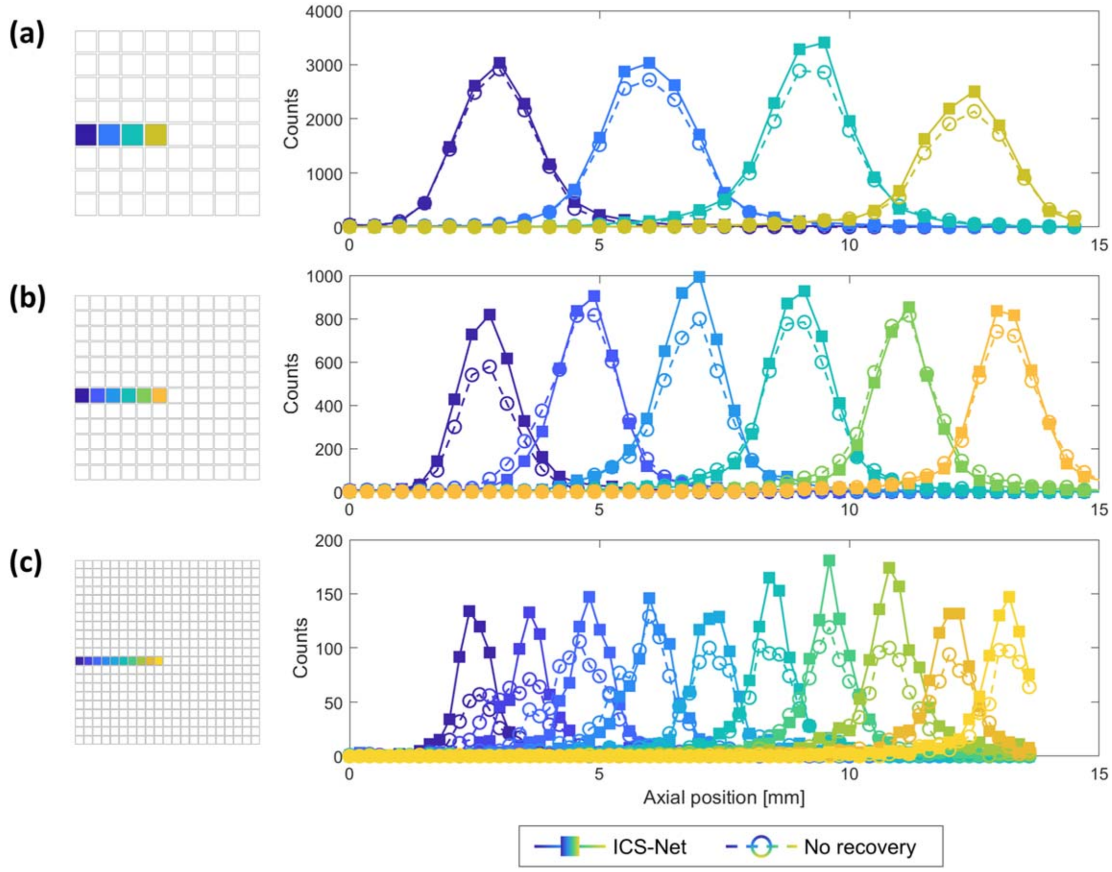

Figure 8. Count profiles of (a) 8 × 8, (b) 12 × 12, and (c) 21 × 21 arrays obtained from the experimental measurement of intrinsic resolution. The colors indicate the row indices of the opposing crystal pairs.

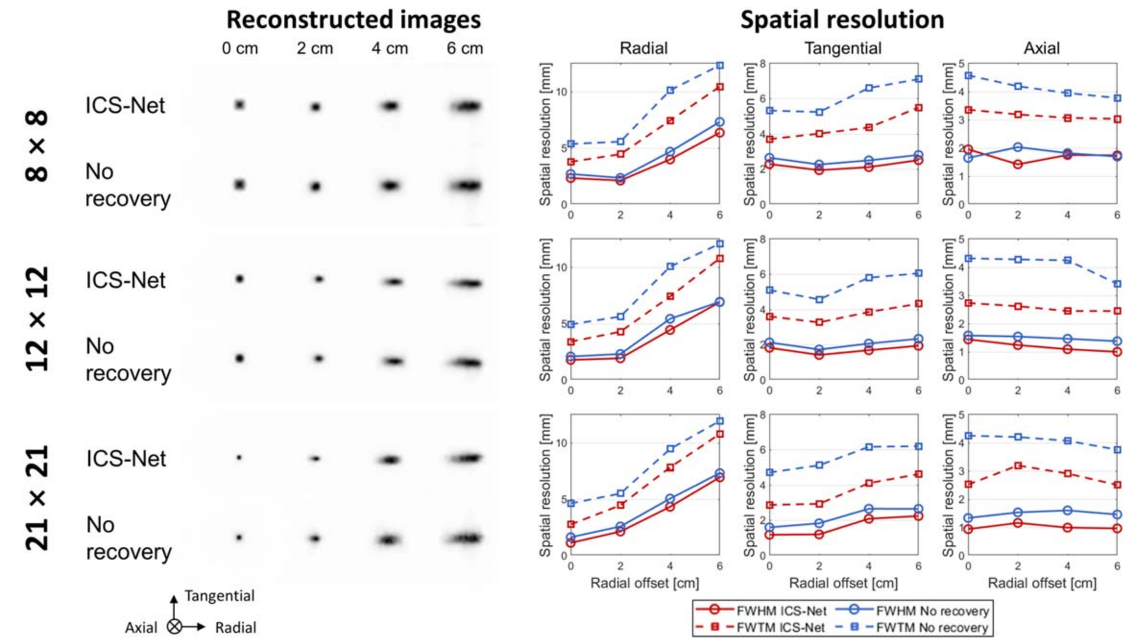

Figure 9. Spatial resolution measurement of the PET rings. (Left) Normalized images of the point source at different radial offsets reconstructed from the virtual PET rings with the 8×8, 12×12, and 21×21 arrays. (Right) Measured FWHM and FWTM of the line profiles along the radial, tangential, and axial directions.

Table 1. Averaged FWHMs and FWTMs over the profiles of the opposing crystal pairs from the intrinsic resolution measurements ($\pm$standard deviation) [mm] and the improvements calculated by equation (4).

	8×8		12×12		21×21	
	FWHM	FWTM	FWHM	FWTM	FWHM	FWTM
ICS-Net	1.95 ± 0.17	3.78 ± 0.18	1.38 ± 0.07	2.85 ± 0.18	0.84 ± 0.08	2.08 ± 0.25
No recovery	1.99 ± 0.17	3.91 ± 0.37	1.45 ± 0.09	3.23 ± 0.36	1.07 ± 0.15	2.53 ± 0.29
Improvement	20%	26%	31%	47%	62%	60%

Table 2. Improvements of volume FWHM by applying ICS-Net compared to the case of no recovery [%].

	0 cm	2 cm	4 cm	6 cm
8×8	11.4	45.9	30.2	20.0
12×12	33.0	44.8	50.0	39.9
21×21	63.9	58.8	58.2	46.8

for the small-pitch array. A similar effect was found for axial blurring but not shown in this paper. As the radial offset increased, the parallax error resulted in a wide point spread along the radial axis as the offset from the center increased, thus minimizing the impact of ICS recovery on the radial resolutions. However, ICS-Net achieved enhancements in the spatial resolution for almost all detector designs and radial offsets. As expected from the simulation and intrinsic resolution results in the previous sections, the 21×21 array showed the largest degree of enhancement compared to the case of no recovery. The volume FWHM improvements defined in equation (6) were significant for the small-pitch arrays in the overall FOV (table 2).

4. Discussion

The spatial resolutions of various light-sharing PET detector designs were improved, which suggests the effectiveness of ICS-Net in recovering ICS events at the detector level. Supervised with the first-interacted rows and columns, the simple-structured CNN learned the patterns of ICS occurrences utilizing small arrays of photosensor output. Monte Carlo simulations were used to measure accuracies, error distances, and intrinsic resolutions, providing evidence for the experimental evaluation of ICS-Net. A relatively small number of parameters are required for the CNN compared to fully-connected networks, which would be advantageous for hardware implementation to process events on-the-fly. A complex network structure would not be beneficial to the accuracy because of the extremely small input size (8×8) in this application.

The ICS-Net was newly designed with a focus on the convenience of training dataset acquisition for real detectors. The benefits of fan-beam irradiation over the pencil-beam were as follows: (1) the number of irradiations was reduced from N^2 to 2 N, (2) a large margin was allowed for precision in geometrical alignment, and (3) only 1D movement of the detector was required. The detector gantry was constructed in a square shape to facilitate switching the irradiating direction between the row and column of the test detector with a single 90-degree rotation. In PET system construction, the time consumption of the supervising task is not expected to be significant if one is equipped with an automated stage and a reference detector containing a thin slab crystal. Another advantage of the electronic collimation setup is the elimination of the need for a heavy mechanical collimator. The simulation results showed that ICS-Net slightly outperformed ICS-cNet in RMSED despite its lower accuracy by individually estimating the row and column indices of the first interaction. As a previous simulation study demonstrated the resolution improvement of a PET ring with ICS-cNet (Lee and Lee 2021), we could predict the effect of applying ICS-Net and support the rationale of conducting the experiments.

For real applications, further considerations in detector engineering would increase the impact of ICS-Net. The performance of ICS-Net would be further improved if one uses a bright scintillator to the increase signal-to-noise level of the detector and highly reflective gap materials to differentiate the energy deposition patterns (Lee and Lee 2021). A low level of noise across the pixels is expected to be beneficial because preserving the scintillation arrival distributions read out by the photosensor array would provide accurate inputs to the network. Philips DPC used in this study was useful to demonstrate the concept in this study, but the detectors were operated under a constant 10 °C, which is impractical for real implementation. Nevertheless, ICS-Net would be implementable to various detectors using multi-channel photosensors (e.g. analog silicon photomultiplier (SiPM) arrays and multi-anode photomultiplier tubes (PMTs)) capable of individual channel readout. Analog SiPMs are widely used at room temperature without significant disruption by dark noise, while PMTs feature noise properties independent of temperature.

Along with the simulations, the experimental results showed that ICS-Net mitigated spatial blurring for all detector arrays, regardless of the location in the FOV. The overall impact of ICS-Net was significant for small-pitch arrays. The intrinsic resolution measurement reflected only the perpendicular irradiation, showing a relatively small impact of ICS-Net for the 8×8 array of which the dimension is widely used in clinical PET. However, the improvements in the volumetric resolution of the 8×8 array were up to 46% in the ring alignment, where a large portion of the photons was obliquely incident. Plus, such ICS recovery would be effective for clinical systems in nuclear medicine using crystal materials with low stopping power (Daube-Witherspoon *et al* 2009, Moskal *et al* 2021), mitigating the effect of a large portion of ICS among the photon interaction (Lee *et al* 2020). The 21×21 array showed the most significant improvement by applying ICS-Net, owing to the largest proportion of ICS among the total events, providing a strong motivation to apply ICS-Net to preclinical and organ-dedicated PET which require sub-mm spatial resolution.

The flood map-based crystal assignment, which was equivalent to the case of no recovery, was highly affected by the quality of the flood map. As shown in figure 4, the peaks appeared indistinct and the events were widely scattered across the flood map of the small-pitch array. While the flood maps only encoded the 1D information of the light distribution by linearly weighting the signal amplitudes to the respective positions of the photosensors, we hypothesized that ICS-Net was capable of recognizing the high-dimensional relationship between the photon interactions and the subsequent photosensor output, resulting in improved performance. The improved spatial resolution offered by ICS-Net would lead to advances in image contrast and lesion detectability (Lee *et al* 2020).

The higher significance of improvement in FWTM resolution than FWHM resolution aligns with previous studies reporting a high contribution of ICS to FWTM (Schmall *et al* 2016) and a large impact of ICS recovery on FWTM (Zhang *et al* 2019). One plausible explanation for these results is that events with large scatter angles and ICS of obliquely incident photons would largely contribute to the peripheral region of the point spread. On the contrary, ICS events with small scatter angles or perpendicularly incident photons are subject to lower crystal misidentification probability, therefore the events are likely to be located in the center of the point spread. We can expect that ICS recovery can particularly improve the contrast of the image by mitigating the broad tail of the point spread function.

The degree of improvement in volumetric resolution was relatively small for the radial resolutions of the peripheral region where the parallax error was dominant over ICS blurring because of the absence of depth-of-interaction (DOI) measurement. DOI capability can improve recovery accuracy by providing additional information on the interaction position (Lee *et al* 2018). Combining DOI information and ICS recovery for real PET detectors remains as a future study.

The crystal length was 20 mm for all arrays in this study to equalize PE absorption and Compton scattering occurrences in the same detector dimension. However, the aspect ratio of the crystal element in the small-pitch arrays was relatively high (e.g. 1.08:20 for the 21×21 array) compared with that of the practical detectors. Therefore, an additional investigation of the degree of improvement is required for systems with different detector geometries.

5. Conclusion

Our proposed ICS-Net successfully enhanced the spatial resolution of PET by learning the first-interacted rows and columns. Prior to the experiments, simulations showed the feasibility of ICS-Net for ICS recovery with high accuracy, reduced mispositioning distance, and enhanced intrinsic resolution for various light-sharing detector designs. Compared with a CNN which required pencil-beams for training dataset acquisitions, the simulations showed that ICS-Net benefitted in reduced tasks with fan-beam irradiations as well as effective error distance reduction. Experimentally trained ICS-N*et* also improved the intrinsic resolution of the detector pair and spatial resolution of the prototype PET ring. With a high impact on small-crystal arrays, ICS-Net is expected to effectively enhance the image quality of high-resolution PET.

Acknowledgments

This work was supported by the Korea Medical Device Development Fund grant funded by the Korea government (the Ministry of Science and ICT, the Ministry of Trade, Industry and Energy, the Ministry of Health & Welfare, the Ministry of Food and Drug Safety) (Project Number: 1711137868, RS-2020-KD000006), and grants from the National Research Foundation of Korea (NRF) funded by the Korean Ministry of Science and ICT (Grant No. 2020M2D9A1093989).

Data availability statement

All data that support the findings of this study are included within the article (and any supplementary information files). Data will be available from 6 February 2023.

ORCID iDs

Seungeun Lee https://orcid.org/0000-0002-5734-5961
Jae Sung Lee https://orcid.org/0000-0001-7623-053X

References

Abbaszadeh S, Chinn G and Levin C S 2018 Positioning true coincidences that undergo inter-and intra-crystal scatter for a sub-mm resolution cadmium zinc telluride-based PET system *Phys. Med. Biol.* **63** 025012

Arabi H, AkhavanAllaf A, Sanaat A, Shiri I and Zaidi H 2021 The promise of artificial intelligence and deep learning in PET and SPECT imaging *Phys. Med.* **83** 122–37

Berg E and Cherry S R 2018 Using convolutional neural networks to estimate time-of-flight from PET detector waveforms *Phys. Med. Biol.* **63** 02LT01

Conti M 2011 Focus on time-of-flight PET: the benefits of improved time resolution *Eur. J. Nucl. Med. Mol. Imaging* **38** 1147–57

Daube-Witherspoon M E, Surti S, Perkins A, Kyba cc M, Wiener R, Werner M E, Kulp R and Karp J S 2009 The imaging performance of a LaBr3-based PET scanner *Phys. Med. Biol.* **55** 45

Gong K, Berg E, Cherry S R and Qi J 2020 Machine learning in PET: from photon detection to quantitative image reconstruction *Proc. IEEE* **108** 51–68

Gonzalez-Montoro A, Gonzalez A J, Pourashraf S, Miyaoka R S, Bruyndonckx P, Chinn G, Pierce L A and Levin C S 2021 Evolution of PET detectors and event positioning algorithms using monolithic scintillation crystals *IEEE Trans. Radiat. Plasma Med. Sci.* **5** 282–305

Gu Y, Pratx G, Lau F W Y and Levin C S 2010 Effects of multiple-interaction photon events in a high-resolution PET system that uses 3D positioning detectors *Med. Phys.* **37** 5494–508

Hsu D F C, Freese D L, Innes D R and Levin C S 2019 Intercrystal scatter studies for a 1 mm 3 resolution clinical PET system prototype *Phys. Med. Biol.* **64**

Hwang D, Kang S K, Kim K Y, Choi H, Seo S and Lee J S 2021 Data-driven respiratory phase-matched PET attenuation correction without CT *Phys. Med. Biol.* **66** 115009

Jan S *et al* 2004 GATE: a simulation toolkit for PET and SPECT *Phys. Med. Biol.* **49** 4543

Kang H G, Nishikido F and Yamaya T 2021 A staggered 3-layer DOI PET detector using BaSO4 reflector for enhanced crystal identification and inter-crystal scattering event discrimination capability *Biomed. Phys. Eng. Express* **7** 035018

Kang S K, Choi H and Lee J S 2021 Translating amyloid PET of different radiotracers by a deep generative model for interchangeability *Neuroimage* **232** 117890

Kim J Y, Suh H Y, Ryoo H G, Oh D, Choi H, Paeng J C, Cheon G J, Kang K W and Lee D S 2019 Amyloid PET quantification via end-to-end training of a deep learning *Nucl. Med. Mol. Imaging* **53** 340–8

Koral K F, Swailem F M, Buchbinder S, Clinthorne N H, Rogers W L and Tsui B M W 1990 SPECT dual-energy-window compton correction: scatter multiplier required for quantification *J. Nucl. Med.* **31** 90–8

Kwon S Il *et al* 2021 Ultrafast timing enables reconstruction-free positron emission imaging *Nat. Photon.* **15** 914–8

Lee M S, Hwang D, Kim J H and Lee J S 2019 Deep-dose: a voxel dose estimation method using deep convolutional neural network for personalized internal dosimetry *Sci. Rep.* **9** 10308

Lee S, Kim K Y, Lee M S and Lee J S 2020 Recovery of inter-detector and inter-crystal scattering in brain PET based on LSO and GAGG crystals *Phys. Med. Biol.* **65** 195005

Lee S and Lee J S 2021 Inter-crystal scattering recovery of light-sharing PET detectors using convolutional neural networks *Phys. Med. Biol.* **66** 185004

Lee S, Lee M S, Kim K Y and Lee J S 2018 Systematic study on factors influencing the performance of interdetector scatter recovery in small-animal PET *Med. Phys.* **45** 3551–62

Levin A and Moisan C 1996 A more physical approach to model the surface treatment of scintillation counters and its implementation into DETECT *IEEE Nucl. Sci. Symp. Med. Imaging Conf.* **2** 702–6

Michaud J B, Tétrault M A, Beaudoin J F, Cadorette J, Leroux J D, Brunet C A, Lecomte R and Fontaine R 2015 Sensitivity increase through a neural network method for LOR recovery of ICS triple coincidences in high-resolution pixelated-detectors PET scanners *IEEE Trans. Nucl. Sci.* **62** 82–94

Miyaoka R S and Lewellen T K 2000 Effect of detector scatter on the decoding accuracy of a DOI detector module *IEEE Trans. Nucl. Sci.* **47** 1614–9

Moskal P *et al* 2021 Simulating NEMA characteristics of the modular total-body J-PET scanner—an economic total-body PET from plastic scintillators *Phys. Med. Biol.* **66** 175015

Muller F, Schug D, Hallen P, Grahe J and Schulz V 2019 A novel DOI positioning algorithm for monolithic scintillator crystals in PET based on gradient tree boosting *IEEE Trans. Radiat. Plasma Med. Sci.* **3** 465–74

Nasiri N and Abbaszadeh S 2021 A deep learning approach to correctly identify the sequence of coincidences in cross-strip CZT detectors *Proc SPIE* **11595** 115953W

Onishi Y, Hashimoto F, Ote K and Ota R 2022 Unbiased TOF estimation using leading-edge discriminator and convolutional neural network trained by single-source-position waveforms *Phys. Med. Biol.* **67** 04NT01

Peng P, Judenhofer M S and Cherry S R 2019 Compton PET: a layered structure PET detector with high performance *Phys. Med. Biol.* **64** 10LT01

Rahmim A, Qi J and Sossi V 2013 Resolution modeling in PET imaging: theory, practice, benefits, and pitfalls *Med. Phys.* **40** 064301

Ritzer C *et al* 2020 Initial characterization of the SAFIR prototype PET-MR scanner *IEEE Trans. Radiat. Plasma Med. Sci.* **4** 613–21

Ritzer C, Hallen P, Schug D and Schulz V 2017 Intercrystal scatter rejection for pixelated pet detectors *IEEE Trans. Radiat. Plasma Med. Sci.* **1** 191–200

Sanaat A and Zaidi H 2020 Depth of interaction estimation in a preclinical pet scanner equipped with monolithic crystals coupled to SiPMs using a deep neural network *Appl. Sci.* **10** 4753

Schmall J P, Karp J S, Werner M and Surti S 2016 Parallax error in long-axial field-of-view PET scanners-a simulation study *Phys. Med. Biol.* **61** 5443–55

Schulze R 2013 PDPC-TEK User Manual Version 0.20

Shao L, Freifelder R and Karp J S 1994 Triple energy window scatter correction technique in PET *IEEE Trans. Med. Imaging* **13** 641–8

Shao Y, Cherry S R, Siegel S and Silverman R W 1996 A Study of inter-crystal scatter in small scintillator arrays designed for high resolution PET imaging *IEEE Trans. Nucl. Sci.* **43** 1938–44

Surti S and Karp J S 2016 Advances in time-of-flight PET *Phys. Med.* **32** 12–22

Surti S and Karp J S 2018 Impact of event positioning algorithm on performance of a whole-body PET scanner using one-to-one coupled detectors *Phys. Med. Biol.* **63** 055008

Teimoorisichani M and Goertzen A L 2019 A study of inter-crystal scatter in dual-layer offset scintillator arrays for brain-dedicated PET scanners *Phys. Med. Biol.* **64** 115007

Ullah M N and Levin C S 2022 Application of artificial intelligence in PET instrumentation *PET Clin.* **17** 175–82

Wu C, Lee M S and Levin C S 2020 Neural network-based inter-crystal scatter event positioning in a PET system design based on 3D position sensitive detectors *IEEE NSS/MIC Conf. Rec.*

Yang J, Xie Y, Xie S, Zhang X, Zhao Z, Weng F, Huang Q, Xu J and Peng Q 2018 Experimental studies of the performance of different methods in the inter-crystal Compton scatter correction on one-to-one coupled PET detectors *IEEE NSS/MIC Conf. Rec.*

Yie S Y, Kang S K, Hwang D and Lee J S 2020 Self-supervised PET denoising *Nucl. Med. Mol. Imaging (2010)* **54** 299

Yoshida E, Kitamura K, Kimura Y, Nishikido F, Shibuya K, Yamaya T and Murayama H 2007 Inter-crystal scatter identification for a depth-sensitive detector using support vector machine for small animal positron emission tomography *Nucl. Instrum. Methods Phys. Res.* A **571** 243–6

Zhang C, Sang Z, Wang X, Zhang X and Yang Y 2019 The effects of inter-crystal scattering events on the performance of PET detectors *Phys. Med. Biol.* **64**